

## SEM-induced shrinking of solid-state nanopores for single molecule detection

This article has been downloaded from IOPscience. Please scroll down to see the full text article.

2011 Nanotechnology 22 425302

(<http://iopscience.iop.org/0957-4484/22/42/425302>)

View [the table of contents for this issue](#), or go to the [journal homepage](#) for more

Download details:

IP Address: 129.6.65.168

The article was downloaded on 26/09/2011 at 17:02

Please note that [terms and conditions apply](#).

# SEM-induced shrinking of solid-state nanopores for single molecule detection

Anmiv S Prabhu<sup>1</sup>, Kevin J Freedman<sup>2</sup>, Joseph W F Robertson<sup>3</sup>, Zhorro Nikolov<sup>4</sup>, John J Kasianowicz<sup>3</sup> and Min Jun Kim<sup>1,5</sup>

<sup>1</sup> School of Biomedical Engineering and Health Science, Drexel University, Philadelphia, PA 19104, USA

<sup>2</sup> Department of Chemical and Biological Engineering, Drexel University, Philadelphia, PA 19104, USA

<sup>3</sup> Physical Measurement Laboratory, National Institute of Standards and Technology, Gaithersburg, MD 20899-8120, USA

<sup>4</sup> Centralized Research Facilities, Drexel University, Philadelphia, PA 19104, USA

<sup>5</sup> Department of Mechanical Engineering and Mechanics, Drexel University, Philadelphia, PA 19104, USA

E-mail: [mkim@coe.drexel.edu](mailto:mkim@coe.drexel.edu)

Received 10 January 2011, in final form 5 August 2011

Published 22 September 2011

Online at [stacks.iop.org/Nano/22/425302](http://stacks.iop.org/Nano/22/425302)

## Abstract

We have investigated the mechanism by which the diameter of solid-state nanopores is reduced by a scanning electron microscope. The process depends on beam parameters such as the accelerating voltage and electron flux and does not involve simple electron-beam-induced deposition of hydrocarbon contaminants. Instead, it is an energy-dependent process that involves material flow along the surface of the nanopore membrane. We also show that pores fabricated in this manner can detect double stranded DNA.

(Some figures in this article are in colour only in the electronic version)

## 1. Introduction

Over the past 15 years, nanometer-sized pores in insulating membranes have received considerable attention as platforms for single molecule detection and analysis [1–5]. Though most of these setups make use of protein ion channels (e.g., *Staphylococcus aureus*  $\alpha$ -hemolysin [6]) suspended in a planar lipid bilayer [7], solid-state nanopores fabricated in silicon-based, free-standing thin films have emerged as promising alternatives due to advantages such as mechanical robustness, tunable diameters, and potentially greater stability under wider ranges of pH, temperature, and salinity. However, efficiently and reproducibly fabricating solid-state pores of desired sizes with low tolerances is still challenging.

Several groups used beams of accelerated electrons or ions (e.g., a transmission electron microscope (TEM) or a focused argon ion beam) to fabricate pores in ultra-thin, free-standing, solid-state ‘membranes’ [8–10]. It was also shown that the nanopore diameter can be either decreased or enlarged with a TEM [8, 9]. The ability to change the pore diameter was attributed to transient softening of the ultra-thin film

and the subsequent surface-tension-driven deformation of the pore to minimize its surface free energy. The extent of the effect depended on the original pore diameter and film thickness [8]. For a membrane of a given thickness, pores below a critical diameter would shrink, whereas larger pores would expand. This technique was further developed by Kim *et al*, who showed that the change in pore diameter was a function of the electron flux and that the internal profile of TEM shrunk pores could be determined [9]. Similarly, the fabrication of nanopores with focused ion beams has also been investigated [10–12]. Li *et al* showed that, by manipulating the flux of ions and the ambient conditions, it was possible to first create a pore in a Si<sub>3</sub>N<sub>4</sub> thin film and then either grow or shrink it to the desired size. The ability to manipulate the pore diameter was attributed to a net result of two competing ion-beam-induced phenomena; the incident ions could either sputter additional molecules from the membrane or create mobile adatoms that were able to migrate along the membrane surface to the periphery of the pore. By manipulating ambient conditions either of these phenomena could be made to dominate, resulting in either pore

expansion or closure. Still others have shown that it is possible to decrease the diameter of preformed pores with low energy electrons from a scanning electron microscope (SEM) [13–18]. Most of these techniques involve the disassociation of a precursor, by the electron beam, into charged species and the subsequent deposition of these charged compounds around the pore [17, 18]. Some groups have reported direct shrinking of solid-state pores by an SEM even without the introduction of a precursor [13–16], but the mechanism of shrinkage in this case is not well understood. Some attribute the pore shrinkage to membrane softening [14, 15], while others suggest that it is caused by electron-beam-induced deposition of hydrocarbon contaminants present in the SEM chamber [13, 16]. Further, there is little consensus over the reproducibility of the shrinking process and the influence of beam parameters such as the accelerating voltage on the rate of shrinking. Though this lack of information limits the control of pore formation, the ability to directly shrink nanopores with a SEM is an attractive alternative since it requires neither elaborate ion beam sculpting apparatus nor an expensive STEM.

Here, we further develop SEM-induced shrinking of nanopores, as an efficient and reproducible strategy for the fabrication of solid-state nanopores. We begin by identifying key parameters that influence the rate of shrinkage and process reproducibility and go on to characterize the internal geometry and elemental composition of the shrunk pores. We then investigate the mechanism of pore shrinkage, showing that it cannot be explained only by the deposition of charged hydrocarbon contaminants around the pore and evaluate an alternative mechanism involving energy-dependent, material flow along the membrane surface that accounts for electron beam interactions with nanopore membrane. Finally, we demonstrate the ability of SEM-shrunk pores to detect individual double stranded  $\lambda$  DNA molecules, which is comparable to that of pores fabricated by a TEM or by ion beam sculpting.

## 2. Material and methods

### 2.1. Nanopore fabrication and shrinking

The pores used in the current work are drilled in amorphous, free-standing, 50 nm thick, low stress silicon nitride membranes by focused ion beam milling. The membranes were fabricated by first depositing a 50 nm thick layer of silicon nitride on a 340  $\mu\text{m}$  thick silicon wafer by low pressure chemical vapor deposition (LPCVD) at 825 °C, using ammonia and dichlorosilane in a flow ratio of 1:5. The silicon nitride thus formed has a tensile stress in the range of 50–150 MPa. Subsequently, photolithography, deep reactive ion etching (DRIE) and KOH wet etching were used to create 50 nm thick, (50  $\times$  50)  $\mu\text{m}^2$  free-standing silicon nitride membranes atop a silicon support structure. Nanopores were fabricated in these membranes using a beam of gallium ions accelerated at 30 kV in an FEI Strata DB235 focused ion beam, through a 10 pA aperture. Under these conditions, by adjusting the drill time it is possible to reproducibly fabricate round pores with diameters ranging from 50 to >400 nm with a tolerance of  $\pm 10$  nm. Pores thus fabricated were reduced in size under

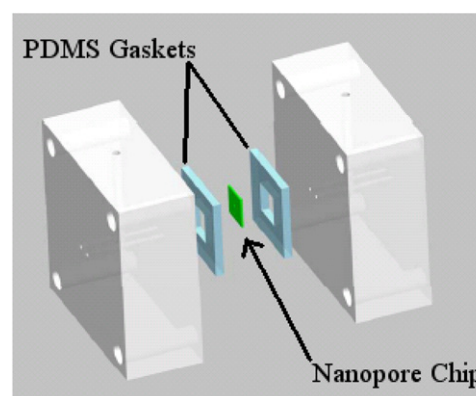


**Figure 1.** A schematic of the polycarbonate flow cell used to house the nanopore chip.

the electron beam of a Zeiss Supra 50VP field emission SEM at various accelerating voltages and imaging magnifications. The elemental composition and morphology of the shrunk walls of the nanopores were further studied by TEM tomography and energy-dispersive x-ray (EDX) analysis using a JEOL JEM2100 TEM operating at an accelerating voltage of 200 kV.

### 2.2. Experimental setup

For single DNA molecule detection, the nanopore-containing chip was cleaned with piranha solution ( $\text{H}_2\text{SO}_4$  and  $\text{H}_2\text{O}_2$  in a ratio of 7:4 volume/volume) for 15 min and housed in a custom-built polycarbonate flow cell with PDMS gaskets as shown in figure 1. Channels were cut in these gaskets to form the electrolytic half cells and Ag/AgCl electrodes, prepared by placing silver wires in bleach overnight, were used to connect the flow cell to the head stage of a patch clamp amplifier (Axopatch 200B, Molecular Devices Inc.). A solution of 1 M KCl and 10 mM Tris buffer was prepared in filtered, deionized water and used as the electrolyte. For detection experiments, a sample of 48.5 kbp  $\lambda$  DNA was diluted from stock to 50 nM in the electrolyte solution, and used as the analyte.  $\lambda$  DNA was used because its detection with solid-state pores is well documented [19, 20].

## 3. Results and discussion

### 3.1. Nanopore shrinking kinetics

We found that, regardless of initial size, the nanopore diameter decreased when imaged in the SEM at accelerating voltages ranging from 10 to 0.5 kV and at magnifications of 10 000 $\times$  (scan area of 11  $\mu\text{m} \times 8 \mu\text{m}$ ) and greater. Figures 2(a)–(c) depicts TEM images of three 115 nm diameter pores that were shrunk by imaging at 1 kV and at magnification of 100 000 $\times$  (scan area of 1.135  $\mu\text{m} \times 0.86 \mu\text{m}$ ) for 0, 5 and 10 s. From these images it is apparent that as the pores are imaged under the SEM a distinct layer, herein referred to as the shrinkage layer, forms along their circumference and develops inwards. The layer appears to be amorphous and, judging from the contrast, has a different thickness and density than the bulk membrane. It was also found that the layer grows uniformly

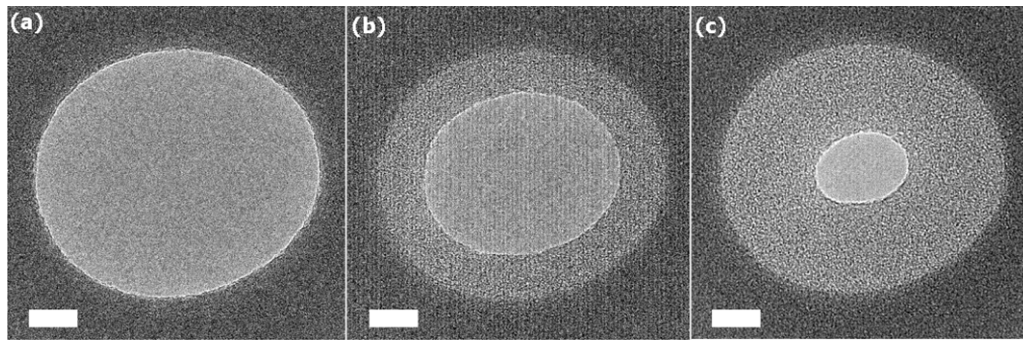


**Figure 2.** TEM images of three 115 nm diameter pores fabricated by FIB milling and shrunk by imaging under the SEM at an accelerating voltage of 1 kV and a magnification of 100 000 $\times$  (scan area of 1.135  $\mu\text{m} \times 0.86 \mu\text{m}$ ) for (a) 0 s, (b) 5 s and (c) 10 s. The scale bar in each figure is 20 nm.

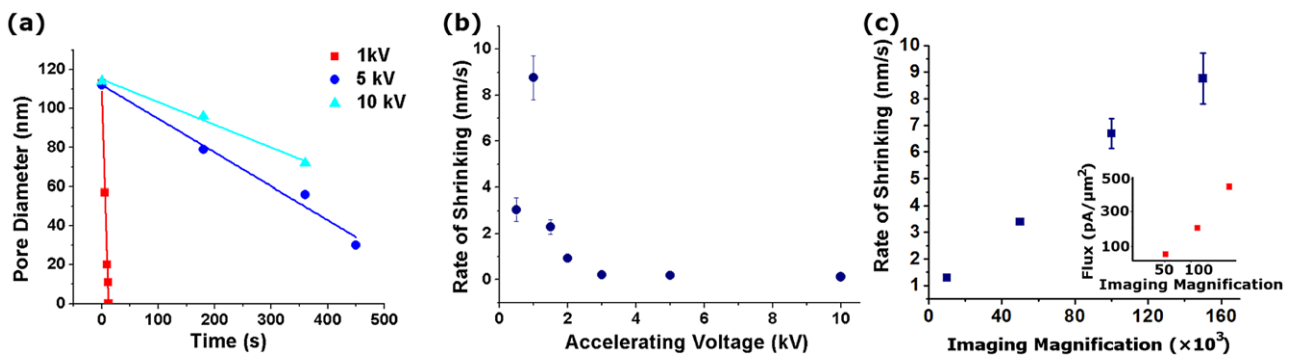


**Figure 3.** Effect of imaging parameters on pore shrinkage. (a) The nanopore diameter decreases linearly with time and the rate of shrinkage remains constant throughout the process. The squares, circles and triangles depict pore diameters while shrinking at 1 kV, 5 kV and 10 kV respectively and at a magnification of 100 000 $\times$ . (b) The shrinkage rate varies with accelerating voltage and is greatest at 1 kV. Shown here are the mean shrinkage rates obtained by shrinking three pores at each accelerating voltage. (c) The rate of shrinkage also increased with increasing magnification due to an increase in electron flux (section 3.2.2) as shown in the inset. Three pores were shrunk at each imaging magnification to determine the mean rate of shrinkage. The error bars in (b) and (c) correspond to the standard deviation of the shrinkage rates under each condition.

from the entire circumference of the pore. In this manner, it is possible to shrink the pores to less than 10 nm in diameter and even close them completely. For all the experiments the electron beam was rastered in such a way that the pore was in the center of the scanned area. The diameter of the pores always decreased linearly with time and the rate of shrinkage was reproducible and a function of beam parameters, such as the imaging magnification and accelerating voltage, that governed the flux of the primary electrons and their interaction with the  $\text{Si}_3\text{N}_4$  thin film (figures 3, 4 and 8).

**3.1.1. Effect of accelerating voltage.** To understand the shrinking process, several pores were shrunk by parametrically varying different beam conditions (figures 3(a)–(c)). We found that the accelerating voltage of the primary electrons greatly influences the shrinking process. As shown in figures 3(a) and (b), the rate of shrinkage is maximum at 1 kV and decreases with increasing accelerating voltage up to 10 kV, beyond which negligible shrinkage was observed. The shrinkage rate also decreases as the accelerating voltage is decreased from 1 to 0.05 kV. Due to the loss of imaging resolution, the shrinkage rate could not be measured accurately at lower accelerating voltages. In all of the above cases, the pores were shrunk by imaging at a magnification of 150 000 $\times$ , such that the

total area scanned was 0.759  $\mu\text{m} \times 0.571 \mu\text{m}$ . While a similar decrease in the accelerating voltage has been reported by Zhang *et al* [15] and Kox *et al* [16], the lowest accelerating voltage they investigated was 5 kV. Moreover, Kox *et al* report a progressive decrease in the shrinkage rate in successive trials even under the same conditions, possibly because of depletion of hydrocarbon contaminants that serve as precursors, but in our case the shrinkage rates remain constant over time.

**3.1.2. Effect of imaging magnification.** The imaging magnification also affects the rate and resolution of the shrinking process. Pores were shrunk at 1 kV and at magnifications ranging from 10 000 $\times$  (scan area of 11.42  $\mu\text{m} \times 8.56 \mu\text{m}$ ) to 150 000 $\times$  (scan area of 0.76  $\mu\text{m} \times 0.57 \mu\text{m}$ ) and the shrinkage rate was found to increase roughly linearly in proportion to the magnification (figure 3(c)). Negligible shrinkage was observed below magnifications of 10 000 $\times$  and sample drift and charging prevented reliable measurements, for pores drilled in bare  $\text{Si}_3\text{N}_4$  membranes, above 150 000 $\times$ . However shrinking of pores drilled in bilayer membranes consisting of a conductive metal layer on top of the silicon nitride was observed even at higher imaging magnifications.

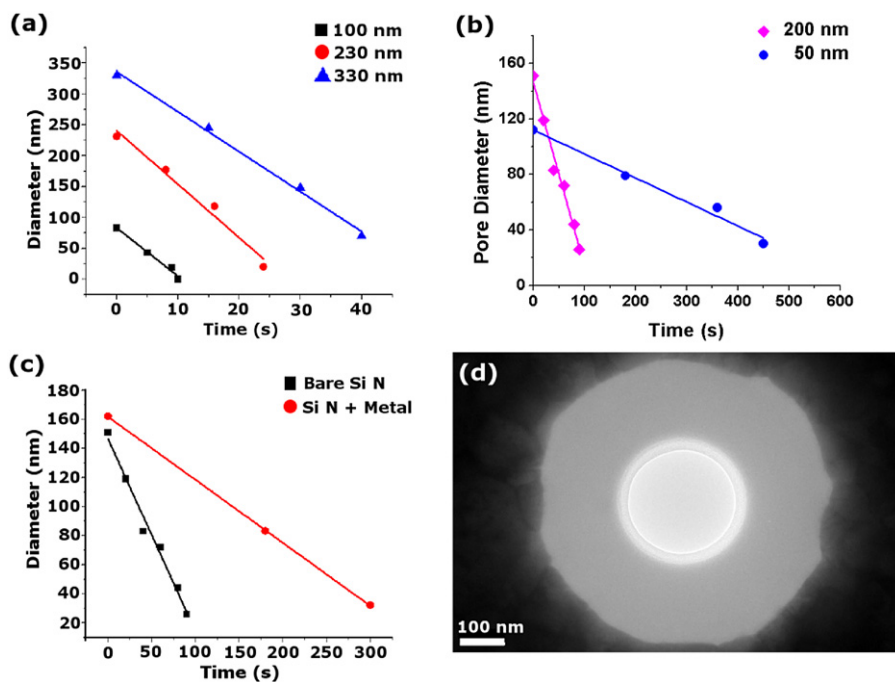


**Figure 4.** The dependence of pore shrinkage rate on pore size and membrane properties. (a) Under fixed accelerating voltage and imaging magnification, the rate of shrinkage is independent of pore size. The squares, circles and triangles depict the shrinkage of pores with initial diameters of 100, 230 and 330 nm at an acceleration voltage of 1 kV and a magnification of 100 000 $\times$ . The rates of shrinkage for these pores are 7.8 nm s<sup>-1</sup>, 8.6 nm s<sup>-1</sup> and 6.5 nm s<sup>-1</sup> respectively. However, the thickness of the nanopore membrane does affect the shrinkage rate. As shown in (b), at 5 kV and a magnification of 100 000 $\times$  the rate increases from 0.2 nm s<sup>-1</sup> for a pore in a 50 nm thick membrane to 1.3 nm s<sup>-1</sup> for a pore in a 200 nm thick membrane. On the other hand, the presence of a metal layer on the membrane decreases the rate of shrinkage (c). One such partially shrunk pore in a metal coated membrane is depicted in (d).

**3.1.3. Effect of pore size.** Unlike in a TEM where both shrinking and enlargement of pores is possible, in the SEM only pore shrinkage is observed and the shrinkage rate is independent of pore size. For pores 100, 230 and 330 nm in diameter shrunk at 1 kV and 100 000 $\times$  the shrinkage rates are 7.8, 8.6 and 6.5 nm s<sup>-1</sup> as presented in figure 4(a). Moreover, unlike the case of ion-beam-induced shrinkage [12] the rate is unaffected by the shrinking history of the pore and hence depends solely on the beam parameters and membrane composition.

**3.1.4. Effect of membrane composition.** In addition to 50 nm thick Si<sub>3</sub>N<sub>4</sub> membranes the shrinkage of pores in bare 200 nm thick Si<sub>3</sub>N<sub>4</sub> membranes and multilayered membranes consisting of 200 nm thick Si<sub>3</sub>N<sub>4</sub> with 20 nm Ti and 100 nm Au was also investigated. At an accelerating voltage of 5 kV and 150 000 $\times$  magnification, the rate of shrinkage increased from 0.2 nm s<sup>-1</sup> for the 50 nm thick membranes to 1.3 nm s<sup>-1</sup> for the bare 200 nm thick membranes (figure 4(b)). Under the same conditions the shrinkage rate for the metal coated membranes was 0.4 nm s<sup>-1</sup> (figure 4(c)). The pores in the multilayered membranes were fabricated in a manner similar to the other pores albeit with longer drill times but, due to different sputtering rates of Au and Si<sub>3</sub>N<sub>4</sub>, pores milled from the metal side had a morphology as shown in figure 4(d), where a few nanometers of the underlying Si<sub>3</sub>N<sub>4</sub> was exposed.

It must be mentioned that one drawback of this technique is that real time visual feedback of the shrinking process

is limited by the resolution of the SEM. For instance, at high accelerating voltages the imaging resolution begins to deteriorate because most of the primary electrons are transmitted through the ultra-thin membranes and fewer secondary electrons are generated. Moreover, the insulating silicon nitride membrane is prone to charging and when imaged at extremely high magnifications there is significant accumulation of charge, which greatly limits the imaging resolution. As a result of these drawbacks it is difficult to reliably image pores smaller than 15–20 nm in diameter with this technique and, while it is still possible to fabricate smaller pores and even completely close the pore, one must rely on shrinkage rates and do so without visual feedback.

### 3.2. Nanopore shrinking mechanism

The most obvious explanation for the shrinkage of pores under the SEM is that the electron beam dissociates hydrocarbon contaminants present in the SEM chamber producing charged species that get deposited inside and around the pore. This has been suggested as the mechanism for shrinkage not only in an SEM [13, 16] but also for TEM-induced shrinkage of nanopores [21]. Hydrocarbon contaminants are low molecular weight compounds whose flux on to the membrane  $f$  is given by  $f \approx \sqrt{\frac{M}{T}} p$ , where  $M$  is the mass of the hydrocarbon molecules,  $T$  is the absolute temperature and  $p$  is their partial pressure [22]. Once adsorbed, these molecules are only loosely

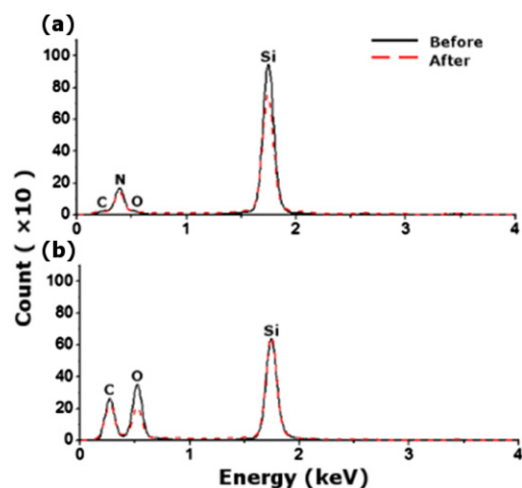


**Figure 5.** The EDX spectrum of (a) the bulk membrane and (b) the shrinkage layer before and after piranha and oxygen plasma treatment.

attached to the surface and may freely migrate along the surface. For stationary beams, focused at a single point, the hydrocarbon contaminants have been shown to migrate toward the beam, forming distinct pillar like structures on either side of the membrane [23]. However, the concentration distribution of different hydrocarbon contaminants depends on a number of factors including sample handling conditions, usage history of the SEM etc and is highly variable. Moreover, when the beam is rastered over a small region for long periods of time, the local concentration of hydrocarbons should rapidly get depleted, thus slowing the rate of adsorption. Yet, we find that our shrinkage rates not only remain uniform throughout the process even for pores with initial diameters as large as 330 nm but the rates are reproducible over time as well. Also, this mechanism fails to account for the observed increase in the rate of shrinkage for the 200 nm thick membranes or the fact that the shrinkage rate is maximum at 1 kV. Moreover, such contaminants are generally deposited uniformly all over the scanned region, yet for our metal coated pores only the  $\text{Si}_3\text{N}_4$  layer shrank while the Au layer remained unaffected (figure 4(d)). It is then obvious that the shrinkage of pores under the SEM cannot be explained by the deposition of hydrocarbon contaminants alone and the mechanism of shrinkage was investigated in further detail.

**3.2.1. Elemental composition and morphology of the shrinkage layer.** Energy-dispersive x-ray spectroscopy (EDX) analysis shows that while the bulk of the membrane primarily consists of silicon and nitrogen with trace amounts of carbon and oxygen, the shrinkage layer contains almost no nitrogen and significantly greater levels of carbon and oxygen with little change in the silicon content. However, treating the shrunk pore with boiling piranha solution ( $\text{H}_2\text{SO}_4$  and  $\text{H}_2\text{O}_2$  in a ratio of 7:4 volume/volume) for 15 min and then subjecting it to oxygen plasma (6.8 W, 101.6 kPa) for 10 min had no effect on the shrinkage layer and its EDX spectrum (figure 5). Only extended oxygen plasma treatment at 18 W, for more than 30 min, was found to have an appreciable effect on the morphology of the shrinkage layer, and even then the layer was not completely destroyed. The fact that the shrinkage layer is not affected by these wet chemistry and plasma surface treatments, which effectively destroy any adsorbed organic contaminants, suggests that, though the shrinkage layer is carbonaceous, the carbon atoms are not simply adsorbed on the surface but must be chemically bonded to it.

TEM tomography was used to track the growth of the shrinkage layer and to determine the internal morphology of the shrunk pores [9, 24, 25]. Pores were fabricated in commercially available  $500 \mu\text{m} \times 500 \mu\text{m}$ , 50 nm thick Dura SiN membranes (Electron Microscopy Sciences) and shrunk by imaging at 1 kV and  $100\,000\times$  magnification for different lengths of time. The rate of shrinkage in these membranes is similar to that in our original membranes and the larger area allowed the pore to be imaged over a greater range of tilt angles, thus providing better resolution in the final tomogram. Figures 6(a)–(c) depict the internal profile of three 120 nm diameter pores shrunk for 0 s, 1 s and 10 s respectively. The tomogram for the pore in figure 6(c) is shown in greater detail in figure 6(d) to highlight the distinct shape of the shrinkage layer. The tomograms are aligned such that in each case the pores were drilled and shrunk from the top surface. The inverted hourglass shape of the walls of the nanopore, as seen in figure 6(a), are a result of the ion beam's Gaussian profile [26] and the lateral diffusion of ions during the drilling process.

Figures 6(a)–(c) show that, as the shrinkage process starts, the shrinkage layer only develops on the top surface and subsequently grows along the walls of the pore, suggesting that a flow of the shrinkage material is involved. Also, this

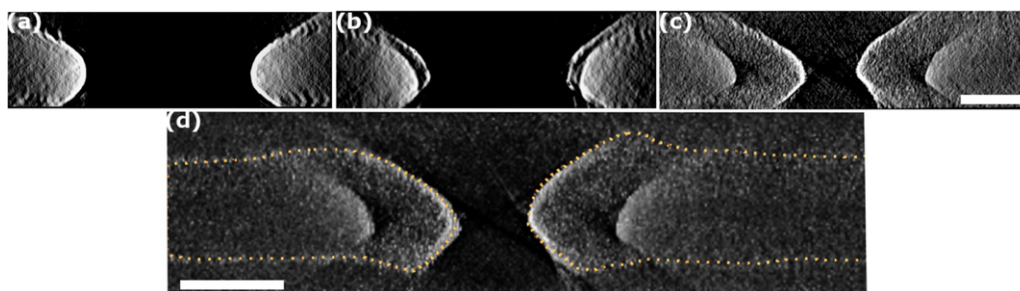


**Figure 6.** Profiles of three 120 nm diameter pores shrunk for (a) 0, (b) 1 and (c) 10 s respectively. The scale bars are 50 nm in length. An enlarged view of the tomogram for the pore in (c) is presented in (d) to highlight the distinct shape of the shrinkage layer. It is interesting to note that there is appreciable aggregation of the shrinkage material only in the vicinity of and inside the pore. The dotted lines in (d) demarcate the edges of the membrane and the pore in the tomogram.

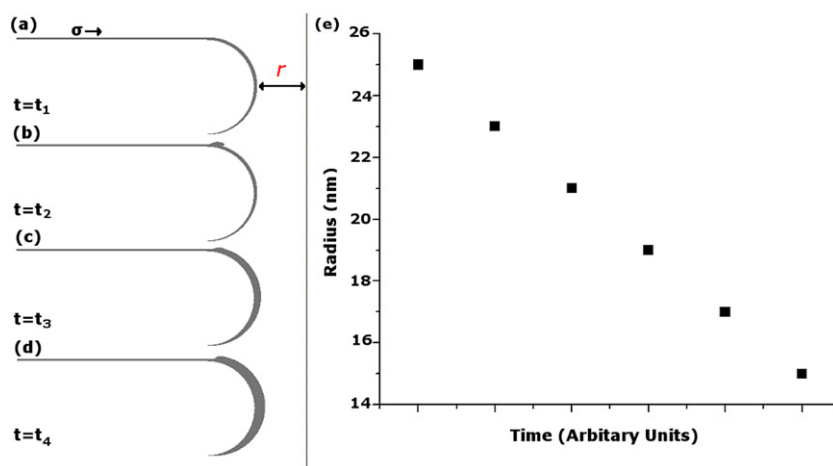


**Figure 7.** The deformation of the theorized viscous layer under the effect of internal stresses is depicted. (a) Illustrates the viscous layer prior to shrinkage with the internal stress  $\sigma$  shown. The thickness of the layer is 1 nm and the radius of the simulated pore is 25 nm. (b)–(d) The formation of the shrinkage layer at arbitrary, but equally spaced, time points  $t_2$ ,  $t_3$  and  $t_4$  where  $t_2 < t_3 < t_4$ . This simple model not only correctly predicts the shape of the shrinkage layer but also shows a linear decrease in the pore radius with respect to time as shown in (e).

layer is distinct from the substrate and the original walls of the pore are still visible in the shrunk pores. As the shrinkage progresses, this layer continues to grow along the walls of the pore, finally converging at the center. It is interesting to note that while the electron beam was rastered over a relatively large area around the pore there is an observable accumulation of the shrinkage material only within the pore and in a narrow region in the vicinity of the pore on the scanned surface as seen in figure 6(d).

**3.2.2. Model for pore shrinkage.** In order to account for our observations of the shrinking kinetics of nanopores and the morphology of the shrinkage layer, we tested a model involving material flow along the membrane surface. We begin by hypothesizing the formation of an amorphous, carbonaceous, viscous, solid layer on the scanned surface of the membrane. Under the effect of the electron beam, due to effects such as Joule heating and charging it is plausible that such a layer might form as a result of carbon incorporation into the amorphous silicon nitride membrane in much the same way as silicon carbon nitride thin films are formed [27] or that the viscous layer is first formed as a result of beam effects and carbon is subsequently taken up. In either case, such a thin film forming on top of a substrate generally develops intrinsic stresses [28], which for an amorphous film on an amorphous substrate may be approximated by  $\sigma = (f - \gamma)/t_0$ , where  $f$  and  $\gamma$  are the surface stress and surface free energy of the thin film material and  $t_0$  is the thickness of the film [29]. Such intrinsic stresses are typically compressive and of the order of a few MPa [28]. In our analysis, we assume that, as the electron beam is rastered on a particular area, such a layer is formed within and around the scanned region with the pore in the center and compressive stresses within this newly formed layer cause it to flow into the pore and gradually shrink it.

To test this model with finite element analysis in COMSOL, the radially symmetric problem of a pore in the middle of a viscous, solid layer was simplified to the two-dimensional case shown in figure 7(a). For the sake of this

analysis, the thickness of the layer was set as 1 nm, the length of the membrane considered was 100 nm, and the boundary conditions were set such that the top surface of the layer was free to move while the part in contact with the substrate was fixed. Moreover, the internal stress of the layer was modeled as a constant stress along its surface and also normal to the end away from the pore. Typical values in the range of 1–100 GPa were assumed for the elastic modulus  $E$  and the shear modulus  $G$ . Both these parameters were considered isotropic, and the deformation of the layer under the constant stress was simulated. As shown in figures 7(b)–(d), this simple model accurately depicts the general shape of the shrinkage layer and its development over time and also predicts a linear decrease in the pore radius with respect to time (figure 7(e)), which is obtained by measuring the thickness of the shrinkage layer at the narrowest point on the pore profile. In several simulations, for various values of  $E$  and  $G$ , while the general shape of the shrinkage layer remained the same, the rate of shrinkage was greatly influenced by these material parameters. This led to a second assumption that, while these parameters may remain constant during pore shrinking, their values are determined by the interaction of the electron beam with the nanopore membrane, such that greater energy transfer between the electron beam and the membrane would lead to a less stiff layer, thus resulting in faster shrinkage. The interaction of incident electrons with our free-standing membranes was hence further explored.

When accelerated electrons impinge on a substrate they undergo either elastic or inelastic collisions with the substrate's atoms. While there is negligible transfer of energy in the case of elastic collisions, inelastic collisions, which are more probable for low atomic number substrates, lead to energy transfer from the electrons to the substrate [30]. This decreases the kinetic energy of the electrons and hence their penetration depth into the substrate. The total energy absorbed by the membrane [31] is  $E_A = E_0 - \eta_T E_T - \eta_B E_B$ , where  $E_0$ ,  $E_T$  and  $E_B$  are the energies of the primary, transmitted

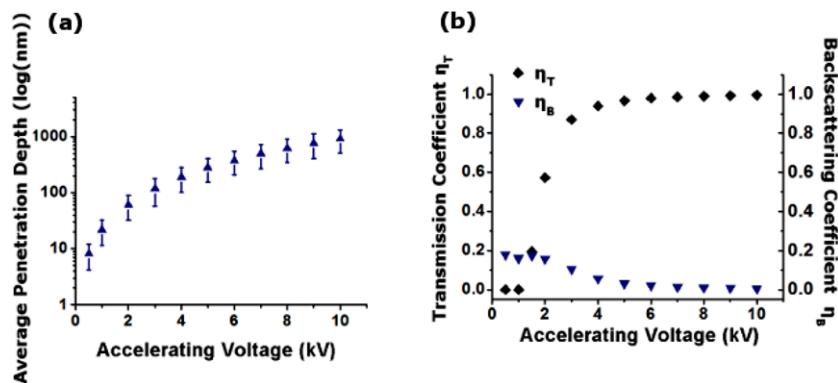


**Figure 8.** Monte Carlo simulations were performed using CASINO to determine (a) the average penetration depth of the electrons within a silicon nitride substrate at various accelerating voltages and (b) the fraction of electrons transmitted through and backscattered by a 50 nm thick silicon nitride membrane. The penetration depths in (a) were determined by simulating the electron collision cascade generated by 100 000 electrons. The distribution of the electron penetration depths within the substrate follows a Gaussian distribution and the error bars indicate the FWHM of the distribution.

and backscattered electrons respectively,  $\eta_T$  is the fraction of electrons transmitted through the membrane and  $\eta_B$  is the fraction of electrons backscattered. Monte Carlo simulations were performed using CASINO modeling software [32] to determine the transmission and backscattering efficiencies (figure 3(c)) in a 50 nm thick silicon nitride membrane as well as the penetration depth of the electrons (figure 8) within a silicon nitride substrate, at various accelerating voltages.

The simulations show that, although  $\eta_B$  decreases slightly with increasing accelerating voltage, it remains relatively low throughout the range of simulated voltages. On the other hand, at accelerating voltages below 1 kV, the depth of electron penetration into the substrate is less than the thickness of the membrane and hence  $\eta_T$  is negligible, and as a result most of the energy of the primary electrons is dissipated within the membrane. However, as the accelerating voltage is increased, the electron penetration depth increases beyond the thickness of the membrane and hence  $\eta_T$  rises rapidly. As a result, at higher accelerating voltages, less energy is absorbed by the membrane. Thus, the peak in the rate of shrinkage at 1 kV is a result of the optimum absorption of electron energy by the 50 nm thick silicon nitride membranes. Similarly, for a membrane of a different thickness the optimal shrinkage rate will be achieved at an accelerating voltage where the electron penetration depth is equal to or slightly less than the thickness of that membrane. As in the case of the 200 nm thick membrane, because the penetration depth of 5 kV electrons into the substrate is less than 200 nm,  $\eta_T$  remains negligible for these membranes and the total energy absorbed is much greater than that for 50 nm thick membranes, thus accounting for the observed increase in the shrinkage rate (figure 4(b)). Likewise, in the Au coated membranes, the higher stopping power of Au decreases the amount of electrons reaching the underlying  $\text{Si}_3\text{N}_4$ , thus accounting for the decrease in the rate of shrinkage (figure 4(c)). Similarly, the linear dependence of the rate of shrinkage on the magnification can be explained by an increase in the electron flux, because at higher magnifications the beam diameter and imaged area decrease progressively while the beam current remains constant. The current at 1 kV, measured

using a Faraday cup, is 190 pA, and the increase in electron flux with magnification corresponds to the observed increase in the rate of shrinkage (figure 3(c) inset).

Based on this analysis, it is possible to explain the shrinking of nanopores under the SEM by an energy-dependent process involving material flow along the membrane surface, by assuming the formation of a carbonaceous shrinkage layer whose material properties are functions of the energy absorbed by the membrane. This energy is given by  $E_{\text{total}} = (\int_0^T E_A(V, z) dz) j(M, \tau)$ , where  $T$  is the membrane thickness,  $M$  and  $\tau$  are the magnification and scan time per frame, which determine the electron flux  $j$ , and  $V$  is the accelerating voltage that governs the amount of energy  $E_A$  deposited per unit depth  $z$  per electron [31].

Partial validation of this model was achieved by simultaneously shrinking a  $5 \times 5$  array of 150 nm pores at 1 kV and  $20\,000\times$  magnification. The pores were fabricated in such a way that the distance between the centers of adjacent pores was  $1 \mu\text{m}$ . Considering the existence of our assumed viscous layer around such a nanopore array, it is easy to realize that the stress in the layer would be maximum around the pores in the outer rim and will progressively decrease around pores closer to the center. Moreover, adjacent pores would have to share the shrinkage material, since it would simultaneously be strained in multiple directions. In the actual experiments, in accordance with the model, the pores competed for shrinkage material, and the pores in the corners, that had the greatest access to it, shrank the fastest while the ones toward the center shrank progressively more slowly. Figure 9 depicts the array midway through the shrinking process, with the shrinkage layers colored for clarity. In addition, the differences in rates of shrinkage were also dependent on the distance between the pores, with greater differences observed when the pores were drilled closer together (not shown). Moreover, a practical implication of this experiment is that, though SEM-induced shrinking is an efficient technique to fabricate individual nanopores such as those used for single molecule detection, it cannot be used to simultaneously fabricate arrays

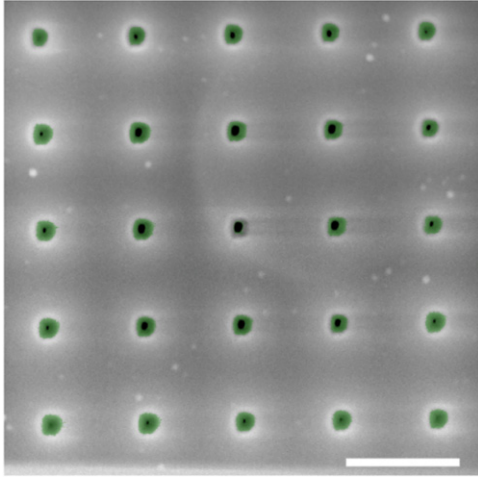


**Figure 9.** A  $5 \times 5$  array of 150 nm pores shrunk simultaneously shows non-uniform shrinkage. The pores at the corners shrink the fastest while those closer to the center shrink progressively more slowly. The shrinkage layers are colored for clarity. The scale bar is 1  $\mu\text{m}$ .

of uniformly sized nanopores, and were such an array to be fabricated the pores would have to be shrunk serially.

### 3.3. Conductance of the nanopore setup

To establish a relation between the conductance of our pores and their geometry, four 150 nm pores were fabricated and shrunk to different diameters. The conductance of each of these pores was estimated by recording the average current through them at applied voltages ranging from  $-150$  to  $150$  mV in steps of 10 mV and determining the slope of the resulting  $I$ – $V$  curve. As shown in figure 10, the  $I$ – $V$  curves for all the pores are linear in this voltage range, which shows that their conductances are constant. Using 1 M KCl and 10 mM Tris, the conductance of a 9 nm, 10 nm, 15 nm and 50 nm pore was found to be  $0.09 \mu\text{S}$ ,  $0.13 \mu\text{S}$ ,  $0.23 \mu\text{S}$  and  $0.64 \mu\text{S}$  respectively.

From figure 6(c) the internal profile of a pore can be described by a hyperbola whose major axis is perpendicular to the pore's axis. The vertices of such a hyperbola are  $(\pm R_{\min}, 0)$  where  $R_{\min}$  is the minimum radius of the pore, measured by the TEM. Also, if the maximum radius of the original pore is  $R_{0,\max}$  and the thickness of the shrinkage layer is  $\Delta R$ , the points  $(\pm R_{\max}, \pm \frac{T}{2})$  would also lie on the hyperbola, such that  $R_{\max} = R_{0,\max} - \Delta R$  is the maximum radius of the shrunk pore and  $T$  is the thickness of the membrane. The equation of such a

hyperbola would then be  $\frac{r^2}{R_{\min}^2} - \frac{t^2}{b^2} = 1$ , where  $b = \sqrt{\frac{R_{\min}^2 (\frac{T}{2})^2}{R_{\max}^2 - R_{\min}^2}}$ . Consequently, the conductance of the pore is given by  $G = \frac{1}{\Omega}$ , where  $\Omega = \frac{2\rho}{\pi R_{\min}^2} \int_0^{\frac{T}{2}} \frac{dr}{(1 + \frac{r^2}{b^2})} + \frac{\rho}{2R_{\max}} = \frac{2\rho b \tan^{-2}(\frac{r}{b})}{\pi R_{\min}^2} + \frac{\rho}{2R_{\max}}$ ,  $\rho$  is the resistivity of the electrolyte and  $\frac{\rho}{2R_{\max}}$  is the access resistance [33]. Given a room temperature resistivity of  $9.5 \Omega \text{ cm}$  for 1 M KCl, the theoretical conductance as a function of  $R_{\min}$  is depicted by the red line in the inset of figure 10 and found to be in good agreement with the experimentally obtained values.

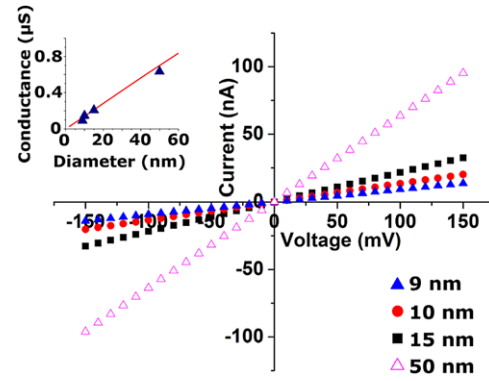


**Figure 10.**  $I$ – $V$  curves for 9, 10, 15 and 50 nm diameter pores in 1 M KCl and 10 mM Tris buffer. In the voltage range from  $-150$  to  $150$  mV, the pores behave like linear resistors with a constant conductance. The triangles in the inset show the conductance of the four pores, averaged over four measurements, as a function of their minimum diameters with the theoretical conductance depicted by the red line. The observed standard deviation for the conductances was  $\pm 0.005 \mu\text{S}$ , thus the error bars are too small to display.

### 3.4. Detecting double stranded DNA

Next, a 15 nm pore, fabricated by shrinking a 150 nm pore at 1 kV and a magnification of  $150\,000\times$ , was used to detect  $\lambda$  DNA. When 50 nM  $\lambda$  DNA was added to the anodic half-cell and a 120 mV voltage bias was applied, transient current drops were observed (figure 11(a)). Each of these current drops is caused by one or more  $\lambda$  DNA molecule being driven through the pore. In order to distinguish these current drops from random fluctuations caused by electromagnetic noise, only events with current drops greater than 100 pA were analyzed. Given the pore size, the  $\lambda$  DNA molecules can be pulled through it in various conformations, each interacting with the pore differently and hence producing a different current signature. Typical ionic current signatures are depicted in figures 11(b) and (c). These current blockades have average amplitudes of 185 pA and 132 pA and are 0.31 ms and 0.5 ms in duration respectively, in good agreement with Chen *et al*, who detected  $\lambda$  DNA through a pore that was 15 nm in diameter and  $\sim 200$  nm in length at a voltage bias of 200 mV [20]. The distributions of the average amplitude and duration of all the current blockade events are shown in figure 11(d) along with the individual histograms for these parameters. For clarity, a contour plot of the region with the most events is presented as the inset. This figure shows two distinct populations of events with current drop values of  $\approx 130$  pA and  $\approx 240$  pA, which might be caused by a single molecule of  $\lambda$  DNA and either a single molecule folded onto itself in different conformations, or multiple molecules translocating simultaneously.

To further characterize  $\lambda$  DNA translocations, the experiment was repeated with a 12 nm and a 20 nm diameter pore. Since the number of conformations a molecule can acquire during translocation depends on the size of the pore, it is expected that the position of the peaks observed in figure 11(d) would be different in the case of different pore sizes. Likewise, we find that with increasing pore size the range of the observed current drops increases, as shown in

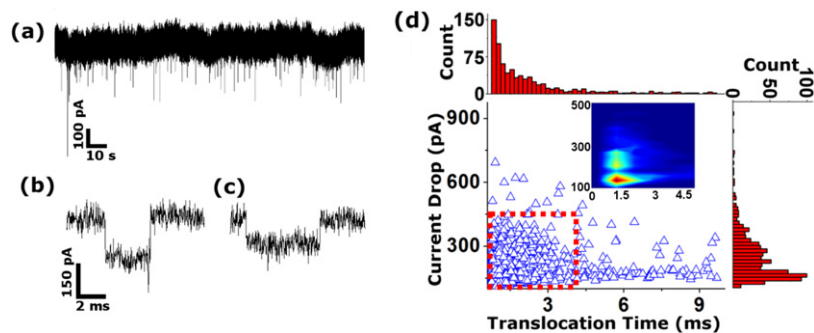


**Figure 11.** Electrical detection of double stranded DNA with the solid-state nanopore. Upon introducing 50 nM of  $\lambda$  DNA into the anodic half-cell and applying a 120 mV voltage bias, transient current drops were observed as depicted in (a). These current drops were not observed in the absence of the analyte and are thus believed to be caused by the  $\lambda$  DNA molecules being driven through the pore. The current blockade amplitude and duration are indicative of the conformation of the molecule threading through the pore. (b) and (c) depict typically observed current blockade events. Frequency distributions of the duration and average amplitude of the observed current blockades for  $\lambda$  DNA are shown in (d), with the inset showing a contour plot of the region with the highest number of events.

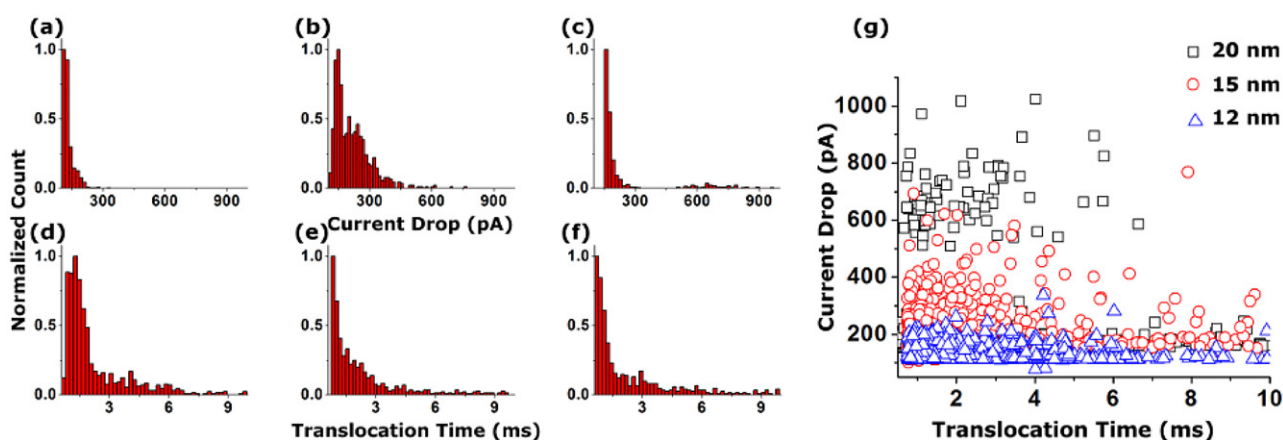


**Figure 12.** Statistical analysis of translocation events. Distributions of the average amplitude of the observed current blockades by  $\lambda$  DNA for the 12 nm, 15 nm and 20 nm pores are shown in (a)–(c) respectively and the corresponding distributions of the event durations are shown in (d)–(f), with the frequency counts normalized for comparison. While the pore size has little effect on the distribution of translocation times, the number of conformations a  $\lambda$  DNA molecule may acquire while translocating the pore increases with increasing pore size. As a result, for the 15 and 20 nm pores, the current drop data show a greater range of current drop values. This is also evident from (g), where the squares, circles and triangles depict translocation events through a 20 nm, 15 nm and 12 nm pore respectively.

figures 12(a)–(f), while there is little change in the distribution of translocation times. Further, multiple peaks are absent from the distribution of current drop values for the 12 nm pore (figure 12(a)), while in the case of the 20 nm pore the second peak is at  $\approx 700$  pA (figure 12(b)). Interestingly, in all three cases the most commonly observed current drop value ( $\approx 150$  pA) is the same. Thus, this peak most likely corresponds to a single  $\lambda$  DNA molecule translocating the pore and the additional peaks observed in case of the 15 and 20 nm pores are caused by a single molecule folded onto itself, multiple molecules translocating the pore simultaneously or combinations thereof. Moreover, the similar distribution of translocation times for all the three pores suggests that either there is little difference between how these conformations interact with the walls of the pore or that the timescale of these interactions is much larger than the amount of time it takes for them to travel across the pore.

These results suggest that SEM shrunk pores are comparable to solid-state pores fabricated by other techniques

in terms of detecting individual  $\lambda$  DNA molecules. In the future, we aim to further investigate the effect of the composition of the shrinkage layer on the translocation kinetics of different molecules and characterize pore-analyte interactions by varying the size and surface properties of the pore.

#### 4. Conclusion

We have further developed and characterized in detail SEM-induced shrinking of solid-state nanopores as an inexpensive and efficient technique for nanopore fabrication. A parametric study of the different factors that influence the process reveals that the shrinking of pores cannot be explained by deposition of hydrocarbon contaminants alone. Though elemental analysis reveals that the material flowing into the pore and shrinking it is carbonaceous in nature, the internal profile, obtained by TEM tomography, and observed shrinking kinetics are not consistent with a deposition based process. Instead, we find that, by assuming the existence of a thin viscous solid

layer whose material properties depend on energy exchange between the electron beam and the membrane, it is possible to accurately describe the growth of the shrinkage layer and to determine its dependence on various beam parameters and membrane properties. The detection of double stranded  $\lambda$  DNA with single molecule resolution using these pores is also demonstrated.

Hence, this technique can be used to rapidly fabricate nanopores, in a variety of sizes, for single molecule detection and analysis. Moreover, the internal profile of the pores, obtained by TEM tomography, will help refine simulations of the electric field and the nanofluidic environment around the pore [34] and provide a better understanding of how analytes translocate across it. Also, the difference between the elemental composition of the shrunk pores and the bulk membranes as well as the morphology of pores fabricated in multilayer membranes could allow preferential chemical modification of the walls of the nanopore for specific applications.

## Acknowledgments

This work was supported in part by the Human Frontier Science Program Young Investigator Award RGY0075/2009-C, the NIST Office of Law Enforcement Standards and the Telemedicine & Advanced Technology Research Center. The authors are also thankful to Dr Craig L Johnson and Dr Edward Basgall at the Centralized Research Facilities, Drexel University, for their valuable insights. The authors would also like to acknowledge U Kei Cheang, Department of Mechanical Engineering and Mechanics, for his valuable insights. The identification of commercial materials and their sources is given in describing the experimental results. In no case does this identification imply recommendation by the National Institute of Standards and Technology, nor does it imply that the material is the best available.

## Supporting Information

A video of a 400 nm diameter pore being shrunk in real time is provided.

## References

- [1] Kasianowicz J J *et al* 2008 Nanoscopic porous sensors *Annu. Rev. Anal. Chem.* **1** 737–66
- [2] Mulero R *et al* 2010 Nanopore-based devices for bioanalytical applications *J. Assoc. Lab. Autom.* **15** 243–52
- [3] Dekker C 2007 Solid-state nanopores *Nature Nanotechnol.* **2** 209–15
- [4] Howorka S and Siwy Z 2009 Nanopore analytics: sensing of single molecules *Chem. Soc. Rev.* **38** 2360–84
- [5] Kim M J, Robertson J W F and Kasianowicz J J 2009 Single molecule analysis using single nanopores *Nanofluidic: Nanoscience and Nanotechnology* (Cambridge: Royal Society of Chemistry)
- [6] Kasianowicz J *et al* 1996 Characterization of individual polynucleotide molecules using a membrane channel *Proc. Natl Acad. Sci. USA* **93** 13770–3
- [7] Montal M and Mueller P 1972 Formation of bimolecular membranes from lipid monolayers and a study of their electrical properties *Proc. Natl Acad. Sci. USA* **69** 3561–6
- [8] Storm A *et al* 2003 Fabrication of solid-state nanopores with single-nanometre precision *Nature Mater.* **2** 537–40
- [9] Kim M *et al* 2006 Rapid fabrication of uniformly sized nanopores and nanopore arrays for parallel DNA analysis *Adv. Mater.* **18** 3149–53
- [10] Li J *et al* 2001 Ion-beam sculpting at nanometre length scales *Nature* **412** 166–9
- [11] Mitsui T *et al* 2006 Nanoscale volcanoes: accretion of matter at ion-sculpted nanopores *Phys. Rev. Lett.* **96** 036102
- [12] George H B *et al* 2010 Nanopore fabrication in amorphous Si: viscous flow model and comparison to experiment *J. Appl. Phys.* **108** 014310
- [13] Schenkel T *et al* 2003 Formation of a few nanometer wide holes in membranes with a dual beam focused ion beam system *J. Vac. Sci. Technol. B* **21** 2720–3
- [14] Chang H *et al* 2006 Fabrication and characterization of solid-state nanopores using a field emission scanning electron microscope *Appl. Phys. Lett.* **88** 103109
- [15] Zhang W *et al* 2007 Controllable shrinking and shaping of silicon nitride nanopores under electron irradiation *Appl. Phys. Lett.* **90** 163102
- [16] Kox R *et al* 2009 Shrinking solid-state nanopores using electron-beam-induced deposition *Nanotechnology* **20** 115302
- [17] Spinney P *et al* 2010 Nanopore formation by low-energy focused electron beam machining *Nanotechnology* **21** 375301
- [18] Danelon C *et al* 2006 Fabrication and functionalization of nanochannels by electron-beam-induced silicon oxide deposition *Langmuir* **22** 10711–5
- [19] Smeets R *et al* 2006 Salt dependence of ion transport and DNA translocation through solid-state nanopores *Nano Lett.* **6** 89–95
- [20] Chen P *et al* 2004 Probing single DNA molecule transport using fabricated nanopores *Nano Lett.* **4** 2293–8
- [21] Radenovic A *et al* 2008 Fabrication of 10 nm diameter hydrocarbon nanopores *Appl. Phys. Lett.* **93** 183101
- [22] Hren J J, Goldstein J I and Joy D C 1979 *Introduction to Analytical Electron Microscopy* (New York: Plenum)
- [23] Smith D A *et al* 2007 A nanoscale three-dimensional Monte Carlo simulation of electron-beam-induced deposition with gas dynamics *Nanotechnology* **18** 265308
- [24] Patterson N *et al* 2008 Controlled fabrication of nanopores using a direct focused ion beam approach with back face particle detection *Nanotechnology* **19** 235304
- [25] Wu M Y *et al* 2010 TEM study of locally coated nanopore fabricated by ion-beam-induced deposition in a thin membrane *Micron* **41** 609–14
- [26] Tseng A 2004 Recent developments in micromilling using focused ion beam technology *J. Micromech. Microeng.* **14** R15–34
- [27] Lehmann G *et al* 2001 Structure and elastic properties of amorphous silicon carbon nitride films *Phys. Rev. B* **64** 165305
- [28] Ohring M 1992 *The Materials Science of Thin Films* (New York: Academic)
- [29] Mayr S and Samwer K 2001 Model for intrinsic stress formation in amorphous thin films *Phys. Rev. Lett.* **87** 36105
- [30] Goldstein J *et al* 2003 *Scanning Electron Microscopy and X-ray Microanalysis* (Berlin: Springer)
- [31] Kanaya K and Okayama S 1972 Penetration and energy-loss theory of electrons in solid targets *J. Phys. D: Appl. Phys.* **5** 43–58
- [32] Drouin D *et al* 2007 CASINO V2. 42—a fast and easy to use modeling tool for scanning electron microscopy and microanalysis users *Scanning* **29** 92–101
- [33] Hall J 1975 Access resistance of a small circular pore *J. Gen. Physiol.* **66** 531–2
- [34] Prabhu A *et al* 2010 Chemically modified solid state nanopores for high throughput nanoparticle separation *J. Phys.: Condens. Matter* **22** 454107